GEOCHRONOLOGY

Seeing is believing: Visualization of He distribution in zircon and implications for thermal history reconstruction on single crystals

Martin Danišík,[1]* Brent I. A. McInnes,[1] Christopher L. Kirkland,[1,2,3] Brad J. McDonald,[1] Noreen J. Evans,[1] Thomas Becker[4]

Zircon (U-Th)/He thermochronometry is an established radiometric dating technique used to place temporal constraints on a range of thermally sensitive geological events, such as crustal exhumation, volcanism, meteorite impact, and ore genesis. Isotopic, crystallographic, and/or mineralogical heterogeneities within analyzed grains can result in dispersed or anomalous (U-Th)/He ages. Understanding the effect of these grain-scale phenomena on the distribution of He in analyzed minerals should lead to improvements in data interpretation. We combine laser ablation microsampling and noble gas and trace element mass spectrometry to provide the first two-dimensional, grain-scale zircon He "maps" and quantify intragrain He distribution. These maps illustrate the complexity of intracrystalline He distribution in natural zircon and, combined with a correlated quantification of parent nuclide (U and Th) distribution, provide an opportunity to assess a number of crystal chemistry processes that can generate anomalous zircon (U-Th)/He ages. The technique provides new insights into fluid inclusions as potential traps of radiogenic He and confirms the effect of heterogeneity in parent-daughter isotope abundances and metamictization on (U-Th)/He systematics. Finally, we present a new inversion method where the He, U, and Th mapping data can be used to constrain the high- and low-temperature history of a single zircon crystal.

INTRODUCTION

Zircon (U-Th)/He (ZHe) dating is a radiometric dating method based on the ingrowth of ^{4}He from the α decay of U, Th, and Sm. The method has some unique features, which allow it to address a wide range of geological questions on orogenesis, volcanism, landscape evolution, meteorite impact events, ore genesis, basin formation, and sediment provenance (*1*–*8*). Given the rapid diffusion of radiogenic He in zircon at high temperatures, the ZHe method is suited to low-temperature thermochronometry (*9*), recording the time-temperature evolution of zircon-bearing rocks at upper crustal levels [150° to 220°C (*10*); termed the zircon He partial retention zone (ZHePRZ)]. ZHe ages can be determined by measuring bulk He, U, and Th abundances in single zircon crystals (*9*, *11*–*13*) or by in situ laser ablation approaches in which sub-crystal domains are targeted (*14*–*18*). When measured ZHe ages are coupled with a quantitative understanding of He retentivity, not only the timing of cooling but also the rate and style of this cooling through the ZHePRZ can be determined (*10*, *19*–*21*).

Although in many cases the ZHe method has provided ages and thermal histories that are reproducible, geologically reasonable, accurate, and compatible with other chronometers, a number of studies have reported overdispersed or anomalous ages (*22*–*27*) or diffusion behavior that did not follow normal Arrhenius models during step-heating experiments (*9*, *11*, *12*, *28*). Plausible explanations for this included heterogeneous distribution of parent nuclides and fragmentation of crystals (both complicating routine α-ejection correction) (*11*, *21*, *29*–*33*), radiation damage affecting He retentivity and closure temperature (*10*, *34*), and inclusions containing "excess" He (*11*, *35*, *36*). However, to date, our inability to spatially determine the He distribution in dated grains has made interpretation of complex ZHe data equivocal. Understanding the grain-scale He distribution and its relationship to the distribution of parent isotopes could provide a significantly improved understanding of these phenomena and their impact on the (U-Th)/He method.

Here, we describe a new methodology for in situ, high–spatial resolution (micrometer-scale) He analysis based on the combined application of laser ablation microsampling and noble gas mass spectrometry. For the first time, we can visualize the distribution of radiogenic He in minerals and compare it to the distribution of the key parent isotopes (U and Th). Using this approach, we construct high-resolution two-dimensional (2D) images of He abundance variations in a set of zircon crystals, which illustrate the impact of parent isotope zonation, radiation damage, and inclusions on (U-Th)/He systematics. By combining He mapping with other characterization techniques [for example, cathodoluminescence (CL) and Raman microscopy], potential issues associated with undetected fluid inclusions and heterogeneity in both the crystal lattice and the parent nuclide distribution can be better understood. Finally, we present a new procedure for thermal history reconstruction of single zircon crystals, allowing us to constrain the high-temperature history at magmatic temperatures via U-Pb geochronology and the low-temperature history within ZHePRZ via inversion of a directly measured He production-diffusion profile.

RESULTS

We have selected four zircon crystals that illustrate the salient issues arising from heterogeneous distribution of parent nuclides (I2-1, M14-4, and I2-9), intracrystalline variation in radiation damage (I2-9), and the presence of fluid inclusions (R-3) (Table 1). The crystals were extracted from Carboniferous granites from Sardinia (M14-4) and Bohemian Massif (R-3), and from a Proterozoic metagranite from India (I2-1 and I2-9) (Table 1). Representative CL and microscopic images, isotopic

[1]AuScope Australian Geophysical Observing System GeoHistory Facility, John de Laeter Centre, The Institute for Geoscience Research, Department of Applied Geology/Applied Physics, Curtin University, Perth, Western Australia 6102, Australia. [2]Centre for Exploration Targeting, Department of Applied Geology, Western Australian School of Mines, Curtin University, Perth, Western Australia 6102, Australia. [3]Australian Research Council Centre of Excellence for Core to Crust Fluid Systems, New South Wales, Australia. [4]Nanochemistry Research Institute, Department of Chemistry, Curtin University, Perth, Western Australia 6102, Australia.
*Corresponding author. Email: m.danisik@curtin.edu.au

Table 1. Sample details. Origin, ages, internal structures, and α-ejection correction factors of analyzed crystals. F_{th} and F_{tz}, α-ejection correction factors for full crystals with assumed homogeneous and measured zoned distribution of U and Th, respectively, calculated using the equation of Farley *et al.* (*29*); age difference, the difference between the ZHe age corrected for α-ejection based on measured U-Th distribution (termed "true" age here) and the ZHe age corrected for α-ejection assuming homogeneity of U and Th (termed "conventional" age here). "+" and "–" mean that the true ZHe age is older or younger, respectively, than the conventional ZHe age. Ma, million years; N/A, not applicable.

Crystal	Origin	Magmatic/ metamorphic age	Conventional ZHe ages (Ma)	Zircon internal features	F_{th}	F_{tz}	Age difference
I2-9	Leucogranite (India)	Emplacement at 2029 ± 65 Ma; overprint at 536 ± 48 Ma (*53*)	194.7 ± 20.6 to 314.7 ± 18.9 (Table 2)	Oscillatory zoning with two amorphous, inclusion-rich domains, overgrown by thin high–CL response rim; traversed by several radial fractures	0.87	0.82	+5%
I2-1	Leucogranite (India)	Emplacement at 2029 ± 65 Ma; overprint at 536 ± 48 Ma (*53*)	194.7 ± 20.6 to 314.7 ± 18.9 (Table 2)	Oscillatory zoned; low–CL response core with rounded terminations, overgrown by high–CL response rims containing faint indications of patchy and sector zoning	0.88	0.90	–2%
M14-4	Variscan batholith from Sardinia (Italy)	Emplacement at 320–290 Ma (*52*)	67.1 ± 7.1; 73.7 ± 4.2 (Table 2)	Idiomorphically zoned; rim overgrowing high–CL response core with invaginated boundaries	0.78	0.72	+6%
R-3	Variscan granite from Bohemian Massif (Poland)	Emplacement at 312.5 ± 0.3 Ma (*54*)	99.7 ± 6.7 to 271.2 ± 24.8 (*26*)	Oscillatory zoning; low–CL response mineral inclusions; convoluted boundaries between some growth zones	N/A	N/A	N/A

concentration, and U-Pb age maps are presented in Fig. 1; results of conventional ZHe dating are presented in Table 2.

A detailed description of CL patterns (Fig. 1, A, E, I, and M) in the investigated crystals is given in Table 1. Crystal I2-1 is characterized by a low–CL response core (higher U content) and a high–CL response rim (lower U content), whereas crystal M14-4 shows the opposite zonation pattern; crystal I2-9 revealed oscillatory zoning with two amorphous, low–CL response, inclusion-rich domains; crystal R-3 is oscillatory-zoned and contains mineral inclusions.

He abundances measured from single spots within the crystal interiors (that is, regions unaffected by α ejection) range from 0 to ~0.47 ncc (nano–cubic centimeter), and all crystals show strong spatial variation in He distribution that generally correlates well with the CL images (Fig. 1, B, F, J, and N). Domains of high He content correspond to low–CL intensity zones (that is, high U content), and domains of low He content correspond to high–CL intensity zones (that is, low U content). He distribution also correlates with the mapped distribution of parent nuclides [U and Th, expressed in Fig. 1, C, G, K, and O, as eU (effective Uranium) maps, where eU = U + 0.235Th], consistent with the known correlation between CL intensity and U content (*23*, *36*) and the expected correlation between parent and daughter abundance.

However, there are two notable exceptions: First, the He map of crystal R-3 (Fig. 1N) revealed two "hot spots," which have an order of magnitude higher He content (~0.35 and ~0.47 ncc) than other spot analyses (<0.03 ncc) and constitute ~25% of the total He budget in the mapped surface. The position of these hot spots matches the locations of fluid inclusions, which are visible in transmitted and reflected light images (Fig. 1, P and Q), and does not correlate with extreme eU concentrations (Fig. 1O) or the position of mineral inclusions (Fig. 1, M, P, and Q). A backscattered electron image of the ablation surface from one of the hot spot locations (Fig. 1R) revealed an underlying void, presumed to be a fluid inclusion intersected during ablation. It is inferred from these observations that the fluid inclusion was the source of the anomalously high He measured at that location.

Second, the large amorphous domain in crystal I2-9, which is visible in the CL image (Fig. 1I), is characterized by the highest eU within the crystal (Fig. 1K) but does not contain any detectable He (Fig. 1J). This suggests that the advanced degree of structural breakdown of the crystal, as a result of radiation damage, permitted its full complement of radiogenic He to escape. Confocal Raman microscopy quantifies the degree of structural damage and reveals that crystal I2-9 actually consists of several microstructural domains (Fig. 2). When compared to the He map (Fig. 1J), only the domain with the greatest downshift and broadening of the peaks [wavenumber, ~988.9 cm^{-1}; full width at half maximum (FWHM), ~21.6 cm^{-1}] (displayed in blue in Fig. 2, B and C) appears to have lost the ability to retain He, whereas other domains (displayed in red, yellow, and green in Fig. 2, B and C) still retain He despite some degree of radiation damage. This example allows a visual comparison between domains of zircon crystal damage and He abundance, reflecting differential He retentivity as a result of the metamictization process (*10*, *34*). It also confirms that, in addition to U and Th distribution, characterization of the spatial variation of zircon crystallinity before (U-Th)/He analysis could greatly enhance age interpretation (*10*, *37*).

DISCUSSION

This extension of conventional in situ He analysis to the production of He concentration maps in minerals graphically illustrates the impact of inclusions, chemical zoning, and radiation damage on (U-Th)/He dating.

Fluid inclusions as He traps

The He hot spots detected in crystal R-3 show that fluid inclusions in zircon can accumulate significant amounts of radiogenic He. Previous studies (*38*, *39*) have shown that fluid inclusions preferentially trap diffused-in radiogenic He because of its higher solubility in the fluid phase (*38*) and the higher activation energy required for trapped He to migrate across the fluid-mineral interface (*40*). The high He concentrations in the fluid inclusions likely originated from time-integrated capture of radiogenic He

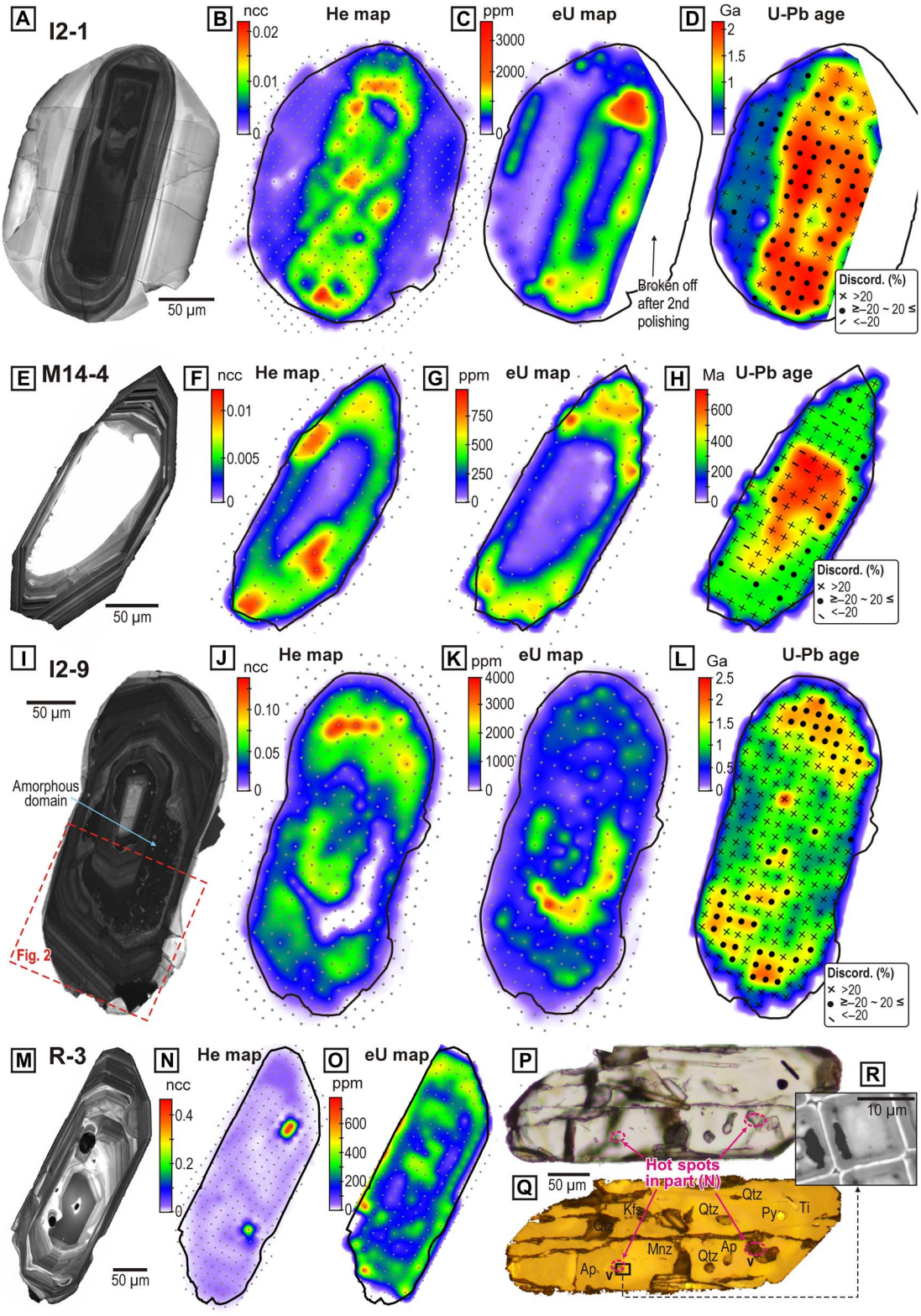

Fig. 1. CL images and isotopic and U-Pb age maps. (**A** to **O**) CL images, He content, eU concentration, and U-Pb age maps (dots mark the center of ablation pits) generated for four representative crystals. ppm, parts per million; Ga, billion years; Ma, million years; ncc, nano–cubic centimeter; Discord, discordance. (**P** and **Q**) Transmitted and reflected light images, respectively, of crystal R-3 showing mineral and fluid inclusions. Mineral inclusions identified by energy-dispersive x-ray analysis include apatite (Ap), K-feldspar (Kfs), monazite (Mnz), quartz (Qtz), and titanite (Ti). Note that the location of the hot spot in the He map (N) corresponds to the location of voids after fluid inclusions (v) in (P) and (Q). (**R**) Close-up secondary electron image of a zircon ablated with square ablation pits. The ablation opened a fluid inclusion, releasing the fluid and leaving an empty cavity (black). Also note that He distribution in all crystals correlates well with CL intensities and eU distributions. Data used for He, eU, and U-Pb maps are shown in tables S1 and S2.

Table 2. Zircon (U-Th)/He data. TAU, total analytical uncertainty; ESR, equivalent sphere radius in micrometers; F_t, α-ejection correction factor calculated using the equation of Farley *et al.* (*29*), assuming homogeneous distribution of U and Th and corrected for the mineral portion removed by polishing. Crystals marked with asterisk were used for isotopic mapping.

Sample code	^{232}Th (ng)	± (%)	^{238}U (ng)	± (%)	^{147}Sm (ng)	± (%)	^{4}He (ncc)	± (%)	TAU (%)	Th/U	Raw age (Ma)	±1 σ (Ma)	ESR (μm)	F_t	Corrected age (Ma)	±1 σ (Ma)
MS14-4*	0.436	1.4	2.904	1.9	0.005	14.0	21.188	1.7	2.5	0.53	57.7	1.5	54	0.86	67.1	7.1
MS14-2	1.445	1.4	2.933	1.9	0.002	17.9	27.100	2.0	2.7	0.49	67.7	1.8	93	0.92	73.7	4.2
I2-1*	0.669	2.0	3.583	2.4	0.007	11.5	94.717	1.6	2.8	0.33	204.2	5.8	150	0.95	215.0	22.8
I2-3	0.420	1.4	0.819	1.9	0.002	24.8	25.475	2.4	2.9	0.51	223.8	6.6	85	0.91	245.4	14.2
I2-6	0.773	2.0	3.684	2.4	0.003	17.6	138.302	2.5	3.3	0.21	286.2	9.6	83	0.91	314.7	18.9
I2-9*	1.407	1.4	2.227	1.9	0.005	14.4	55.975	1.6	2.3	0.53	177.2	4.2	83	0.91	194.7	20.6
R-3*	0.912	2.0	1.671	2.3	0.006	8.6	51.777	2.2	3.1	0.54	221.3	6.8	75	0.90	247.1	14.5
R-3-5	0.149	1.5	0.350	1.9	0.009	12.6	7.954	2.3	2.9	0.42	167.3	4.8	64	0.88	189.6	10.9
R-3-6	0.818	1.4	1.624	1.9	0.006	13.2	46.514	2.0	2.6	0.50	206.6	5.4	91	0.92	225.3	12.7

generated from within the host crystal, although an alternative scenario of trapping parentless He during crystal growth cannot be discounted (*41*).

If all the He trapped within the fluid inclusions (*42*) was produced from radiogenic decay within the crystal, then the calculated whole-crystal ZHe age (247.1 ± 14.5 Ma) (Table 2) would be valid; however, any thermal history reconstruction would require consideration of the differential He retentivity of gas voids and/or fluid inclusions to interpret the age within the closure temperature construct. It has been shown that old samples experiencing complex or slow cooling through the partial retention zone tend to yield less reproducible ZHe ages than young, quickly cooled samples (*24*–*26*). The scatter in (U-Th)/He ages can be reasonably explained by radiation-induced damage (for example, α-recoil tracks and fission tracks) that creates "traps" for He atoms and impedes their diffusion (*40*), essentially resulting in an effective higher closure temperature in inclusion-rich crystals. However, unlike radiation damage, fluid inclusions have less of a spatial relationship with grain-scale crystal chemistry (for example, U and Th content) and thus are unamenable to quantitative modeling.

The He (~1.38 ncc) measured in the hot spots constitutes ~25% of the He budget (5.42 ncc) measured over the analyzed surface and ~2.7% of the total He budget (51.9 ncc) measured in the remaining half of the grain. If the trapped He solely represents parentless He captured during crystal growth, then the two analyzed hot spots would increase the (U-Th)/He age by only ~1%. However, because the entire analyzed grain contained many more inclusions in its 3D volume (Fig. 1, P and Q), the whole-crystal ZHe age of 247.1 ± 14.5 Ma (Table 2) would likely be an overestimate of its cooling age. Hence, fluid inclusions, voids, and fractures trapping He should be considered as an additional explanation for scattered ZHe ages and as a means to understand the commonly observed cryptic relationships between eU and ZHe ages.

Variations in U-Th distribution

Although several methodologies for the characterization of U-Th distribution in (U-Th)/He–dated minerals have been proposed [for example, by fission track and CL imaging, mechanical abrasion, elemental mapping, and depth profiling by laser ablation inductively coupled plasma mass

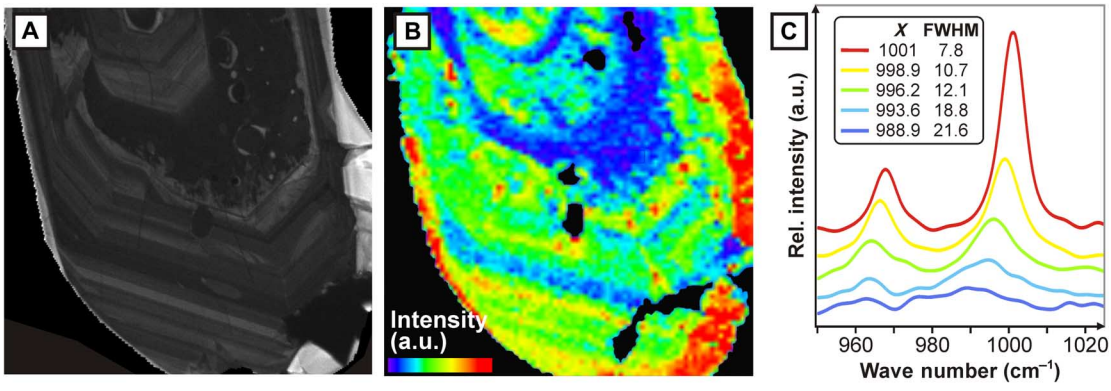

Fig. 2. CL image and Raman spectra. (**A**) Enlarged section of the CL image of crystal I2-9 scanned by Raman spectroscopy (for exact location within the grain, see Fig. 1A). (**B** and **C**) Color-coded Raman map (B) and corresponding Raman spectra (C) showing shift (parameter *X* in the inset) and increased width of peaks (FWHM) in the range of 950 to 1020 cm^{-1}, indicating variable degrees of disorder in the zircon. a.u., arbitrary units. Note that the identified Raman domains correlate with the CL intensities (A) and eU map shown in Fig. 1K. However, the amorphous zone with the most severe radiation damage (blue in the Raman map) has negligible He retentivity and thus shows a negative correlation with the He map (Fig. 1J).

spectrometry (LA-ICPMS) (*22*, *30*, *31*, *37*, *43*–*46*)], the parent distribution is not routinely measured before (U-Th)/He dating, with homogeneous parent isotope distribution assumed during α correction and thermal history modeling. As suggested by others (*9*, *21*, *30*, *31*, *33*, *43*, *44*), the distribution of U and Th is critical to the interpretation of ZHe data for the following two reasons: First, chemically zoned crystals will produce different He diffusion gradients to homogeneous crystals and will undergo differential fractional He loss when cooling through the ZHePRZ. Inverse thermal modeling of ZHe ages generated from zoned and homogeneous crystals has been shown to differ by >30% for complex cooling histories with a protracted residence period in the partial retention zone (*43*, *44*). Second, raw ZHe ages must be corrected for the ejection of α particles along grain perimeters, and the correction factors for homogeneous and zoned zircon (F_{th} and F_{tz}, respectively) differ by up to a few tens of percent (*29*, *30*, *45*).

To demonstrate the effect of U-Th distribution on the F_t correction for the studied crystals, we calculated F_{tz} and F_{th} on the basis of the measured U-Th distribution as shown in eU maps and averaged U-Th concentrations, respectively (Table 1), using the equations of Farley *et al.* (*29*). The difference between F_{tz} and F_{th} (Table 1) ranges from 0.02 (crystal I2-1) to 0.06 (M14-4) and would translate into an age difference of 2 to 6%. Although the magnitude of this age difference is not significant for low-accuracy thermochronology applications, such as calculations of exhumation rates, it may be critically important for high-accuracy applications of (U-Th)/He methods, such as the dating of young volcanic rocks (*47*, *48*), where an offset of eruption age by 6% can significantly change the geological interpretation (*47*). The zircon crystals presented here do not represent extreme examples of U-Th zoning, and calculated differences in α-ejection correction factors for homogeneous and zoned U-Th distributions do not represent worst-case scenarios. Hourigan *et al.* (*30*) argued that the assumption of U-Th homogeneity can result in errors of up to ~30% (in rare cases, higher) for ejection-corrected ages for typical grain sizes and realistic zonation. Moreover, high U-Th concentration zones can result in a high degree of local radiation damage, allowing He to escape from the crystal, in which case a simple α-ejection correction is inappropriate and the error imposed could be close to 100%.

Intracrystal heterogeneity of radiation damage

Intracrystal variation in the degree of radiation damage can result in both positive and negative correlations between eU concentration and He retention (*10*, *40*). The "zero" He zone in the amorphous domain of crystal I2-9 (Fig. 1J) is an area where radiogenic He preferentially escaped due to the presence of fast diffusion pathways. If targeted for in situ (U-Th)/He analysis, a spuriously young ZHe age would be obtained, whereas a younger than expected age would be obtained using the conventional, whole-crystal dating approach.

Because in situ ZHe analysis is performed on polished grain surfaces, it is relatively straightforward to integrate characterization methods with analytical protocols to establish the potential parent isotope zonation (for example, CL imaging and laser ablation map or line scans) and the degree or distribution of radiation damage. We used Raman microscopy to rapidly quantify radiation damage, but CL imaging and electron backscatter diffraction (EBSD) are alternative options.

The complicated intracrystal relationship between eU and He distribution also has implications for the conventional interpretation of ZHe data affected by radiation damage. Previous studies (*9*, *10*) have shown that radiation damage controls the retention of He in zircon in two opposing ways: (i) He loss is prompted at high degrees of radiation damage because He atoms migrate through the interconnected cavities in the crystal lattice, and (ii) at low degrees of radiation damage, He diffusivity decreases because He atoms are "trapped" in damage zones, which obstruct diffusion. Radiation damage thus affects the closure temperature of the (U-Th)/He system and can result in younger or older than expected (U-Th)/He ages. The effect of radiation damage on (U-Th)/He data is commonly evaluated from the relationships between (U-Th)/He ages and eU concentrations measured on whole crystals, an approach that also assumes a homogeneous distribution of radiation damage within the crystals. It is noteworthy that this relationship also serves as a basis for radiation damage/annealing kinetic algorithms used in thermal history modeling (*10*, *49*). Our results for crystal I2-9 show that, at least in this case, the assumption of homogeneity is not met, and the calculation of eU from U and Th concentrations will have an inherent unaccounted uncertainty. However, the combination of He and eU mapping with Raman spectroscopy offers an opportunity to identify individual domains with different degrees of radiation damage and to objectively assess the mutual relationship between radiation damage and He ages.

Finally, the He and eU maps obtained on crystal I2-9 suggests the presence of multiple crystallographic controls on retentivity, which may provide valuable information for the interpretation of diffusion spectra when conducting step-heating experiments. It is commonly assumed that the diffusion domain is the zircon grain itself, which has been demonstrated by diffusion spectra as obeying an Arrhenius relationship. However, some zircon crystals reveal complex diffusion spectra that do not obey a simple Arrhenius relationship (*9*, *12*), suggesting that there may be multiple zones of differential retentivity. Farley (*11*) noted that measuring and understanding He diffusivity parameters in minerals requires the determination of several important parameters, such as grain size and shape, chemical composition, and defect and/or radiation damage density. Given the discussion above, the prevalence of fluid inclusions should also be considered. He mapping, eU mapping, and Raman/CL/EBSD characterization can readily assess all of these parameters.

A novel approach to time-temperature modeling

In addition to addressing important uncertainties in (U-Th)/He analysis, combined He and U-Th mapping offers new capabilities for extracting time-temperature histories. The application of LA-ICPMS to carry out trace element and isotopic mapping allows the collection of all data necessary for U-Pb geochronology and permits the determination of crystallization ages that provide the starting point (or maximum limit) for the subsequent low-temperature history reconstruction. Figure 1 (D, H, and L) and fig. S1 show single-spot U-Pb age maps constructed from the calculated Concordia U-Pb ages, with the degree of discordance in the U-Pb and Pb-Pb isotopic systems symbolized; Concordia diagrams are shown in fig. S1. The U-Pb data suggest crystallization at ~2 Ga (that is, 2016 ± 23 Ma and 1945 ± 63 Ma), followed by a high-temperature thermal event at ~530 Ma (that is, 552 ± 13 Ma and 514 ± 19 Ma) for crystals I2-1 and I2-9, respectively; crystallization at 630 ± 23 Ma, followed by a high-temperature thermal event at 293 ± 3 Ma for crystal M14-4; and crystallization at 322 ± 3 Ma for crystal R-3 (fig. S1). These results agree with previously published U-Pb data for these samples (Table 1) (*50*–*52*) and provide a maximum limit for the corresponding (U-Th)/He ages.

The concomitant application of laser ablation microsampling and noble gas mass spectrometry to map radiogenic He abundance represents the net effect of both He production and diffusion process and provides a novel opportunity to obtain quantitative information on cooling histories from a single grain. Each time-temperature path experienced by a crystal produces a specific He concentration gradient, the shape of which depends on the cooling history (*11*, *21*). Until now, however,

the shape of the He diffusional profile could only be indirectly inferred from step-heating experiments (*11*, *53*), nuclear reaction analysis (*54*), or ^{4}He/^{3}He thermochronometry (*19*–*21*). In situ He mapping offers the possibility of direct measurement of He diffusion profiles. This can be achieved by conversion of He maps into equivalent sphere geometries (*46*, *55*). Bearing in mind the inherent uncertainty in producing 2D He maps, which arise from the redistribution of α particles due to long stopping distances, and the lack of information on α particle distribution in 3D, we note that direct measurement of He production-diffusion profiles and their comparison with modeled production-diffusion profiles offer a new means to obtain cooling histories from zoned zircons.

To demonstrate the feasibility of this new approach, we reconstructed the complete thermal history of crystal M14-4 on the basis of all available data. This crystal was extracted from a Variscan granite of Sardinia, emplaced at 320 to 290 Ma at 3 to 4 kbar (*50*). The apatite fission track age of 48.6 ± 3.0 Ma and the apatite (U-Th)/He ages of 45.1 ± 2.8 to 58.4 ± 3.6 Ma (n = 11) from the same sample [that is, sample S14 in the study of Malusà *et al.* (*56*)] are interpreted to record exhumational cooling of the basement through the apatite fission track partial annealing zone [~120° to 60°C (*57*)] and the apatite He partial retention zone [~40° to 80°C (*58*)] during the Alpine orogeny in the Eocene (*56*).

The high-temperature starting point of the cooling path is defined by U-Pb data recording the crystallization of zircon at magmatic temperatures. Single-spot U-Pb ages from the investigated crystal revealed two significant age components (fig. S1): (i) An older age population of 630 ± 23 Ma corresponding to the high–CL response core is consistent with the timing of the late Neoproterozoic Cadomian orogeny (~650 to 550 Ma), which occurred on the margin of Gondwana and involved collision of several terranes of southern and central Europe. The older ages of the core regions reflect inherited material incorporated into the granite. (ii) The younger U-Pb age population of 293 ± 3 Ma (corresponding to the low–CL response, idiomorphically zoned rim overgrowing the Cadomian core) reflects magmatic crystallization during the Variscan (Hercynian) orogeny, which was caused by continental collision between Laurussia and Gondwana in the Late Paleozoic, leading to the formation of Pangea. Combined, these core-to-rim age relationships define the high-temperature crystallization history of the zircon grain.

For the reconstruction of the low-temperature history, we used the HeFTy program (*59*), which permits modeling of the (U-Th)/He production-diffusion in zircon. We first converted the He, U, and Th concentration maps measured in crystal M14-4 into 1D concentration profiles for an equivalent sphere geometry, according to the procedure of Farley *et al.* (*46*) (Fig. 3, A and C). The U and Th concentration profiles, together with the conventional ZHe age (67.1 ± 7.1 Ma) determined on the remaining part of the crystal and the equivalent sphere radius value calculated based on the size of the crystal, were predefined as input parameters. The starting point of the time-temperature path was set to 900°C at 293 Ma on the basis of the youngest significant U-Pb age component, and its end was set to 10°C at 0 Ma on the basis of the mean annual surface temperature of Sardinia. The algorithm of Guenthner *et al.* (*10*) was opted to model He diffusion in zircon. Using a forward modeling approach, we arbitrarily evaluated three distinct but geologically plausible thermal trajectories that produce a ZHe age of 67.1 Ma, equivalent to the measured ZHe age (Fig. 3, A and C): fast cooling through the ZHePRZ (green line in Fig. 3B), slow cooling through the ZHePRZ (yellow), and a complex thermal trajectory with cooling to surface temperatures at 67 Ma followed by reheating to the ZHePRZ and final cooling (purple). The modeled thermal trajectories result in distinct He diffusional profiles (Fig. 3, A and C), which can then be compared to the measured He diffusional profile to reduce the number of plausible cooling histories. We found that the "green" fast cooling trajectory produces a He diffusional profile that most closely matches the measured He profile (red line in Fig. 3C), whereas the He diffusional profiles from the other two trajectories result in profiles that are inconsistent with the measured result. On the basis of the similarity of measured and modeled He diffusional profiles as well as the agreement of modeled and measured ZHe ages, we suggest that crystal M14-4 cooled through the ZHePRZ at 60 to 70 Ma, corresponding to the latest Cretaceous onset of exhumation of Sardinian basement during the Alpine orogeny (*56*). In addition, this cooling path interpretation finds support in the apatite fission track (48.6 ± 3.0 Ma) and the apatite (U-Th)/He data (45.1 ± 2.8 to 58.4 ± 3.6 Ma), suggesting continuous exhumation cooling until the middle Eocene.

The nonideal fit between the measured and modeled He diffusional profiles may be attributed to (i) the inability to obtain spatial resolutions of less than 9 μm in laser mapping and/or (ii) the overly simplistic assumptions of measured 2D distributions being representative for 3D geometry. Nevertheless, with our new approach, we have demonstrated that from one zircon crystal, it is possible to identify three major orogenic events in Europe (that is, the high-temperature events during the Cadomian and Variscan orogenies and the low-temperature event during the Alpine

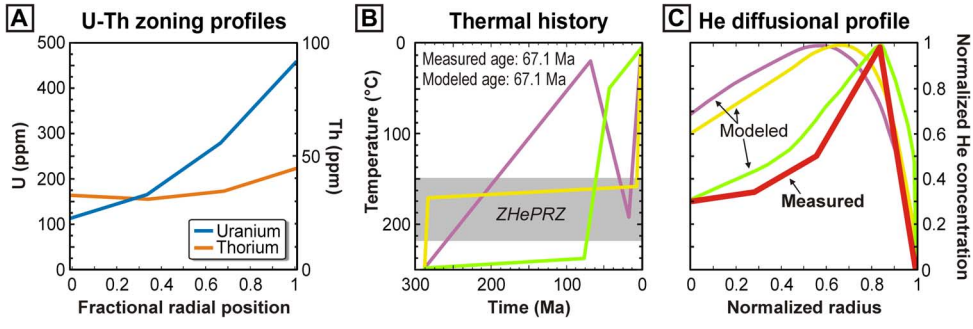

Fig. 3. Thermal history reconstruction. (**A**) Measured U-Th zoning profiles of sample M14-4 used for thermal history reconstruction. Fractional radial position: 0 corresponds to crystal core and 1 corresponds to crystal rim. (**B**) Thermal histories resulting in a ZHe age of 67.1 Ma, illustrating different styles of cooling: fast cooling through the ZHePRZ (green), slow cooling through the ZHePRZ (yellow), and a reheating to the ZHePRZ temperatures (purple). (**C**) He production-diffusion profiles calculated by the HeFTy software (*59*) using the diffusion algorithm of Guenthner *et al.* (*10*) corresponding to the thermal trajectories from (B) (color-coded). Red curve represents the He production-diffusion profile calculated from the measured He map. Note that the green curve [fast cooling through the ZHePRZ in (B)] is most similar to the red curve, suggesting that the fast cooling thermal trajectory is the most viable solution.

orogeny). Therefore, although further work is needed to develop this approach into a robust modeling procedure, the direct measurement of He profiles and comparison with modeled production-diffusion profiles, together with the ability to determine U-Pb ages as a by-product of U-Th mapping, may offer a new means to obtain more accurate and more complete cooling histories from individual zircon grains.

We present the first study on quantitative visualization of the intragrain distribution of He in zircon, aiming to visualize and potentially better understand the peculiarities of the (U-Th)/He system in zircon. This new methodology allows He to be measured at the 0.001 ncc level with a precision of <6% (1 σ) from ~2-μm-deep ablation pits, yielding 2D He maps with spatial resolutions of 9 to 13 μm. Further, it allows direct measurement of ^{4}He production-diffusion profiles, which are diagnostic for the style of cooling minerals experienced within the He partial retention zone. Lastly, part of the methodology proposed here includes mapping of the intragrain distribution of U and Th by LA-ICPMS, allowing a more comprehensive calculation of α-ejection correction.

Using this method, we have constructed He maps for selected case-study zircon crystals. Comparison of the He maps with CL and optical microscopy images, Raman spectra, and trace element maps demonstrates that the variability in He abundance correlates with the spatial distribution of the parental U-Th radionuclides, with fluid inclusions, and with radiation damage that can increase or decrease He retentivity. These complexities may contribute to the dispersion of ZHe ages commonly observed in old, slowly cooled samples; help to explain the inaccuracy sometimes observed in thermal history models; or help to explain non-Arrhenian diffusion behavior in some samples.

The observation that intracrystalline voids, such as fluid inclusions, contain two to three orders of magnitude more He than the surrounding crystal is notable, particularly because this represents the time-integrated capture of radiogenic He as it transits through the crystal during diffusion. If undetected and pervasive in measured grains, these inclusions could contribute to scattered ZHe ages and complex eU-age relationships and/or affect He diffusion kinetics.

Finally, 2D He mapping capability offers a new means for quantitative thermal history reconstruction on single crystals. The thermal history at magmatic temperatures is constrained by U-Pb data obtained as a by-product of U-Th mapping, and the low-temperature thermal history is reconstructed from ZHe age data and the equivalent sphere He diffusional profile approximated from the directly measured 2D He map. Using this approach, we deciphered the imprint of three major European orogenic events (Cadomian, Variscan, and Alpine) in a single zircon crystal from Sardinia. Although further work is needed to develop this approach into a robust modeling procedure, the possibility of direct measurement of He production-diffusion profiles may offer a new avenue for more robust thermal history reconstruction from (U-Th)/He data.

MATERIALS AND METHODS

Zircon (Table 1) was extracted from a Proterozoic metagranite from India (*51*) and Carboniferous granites from Sardinia and Bohemian Massif (*50*, *52*). The relatively coarse size of the crystals (>100 μm in diameter) and their elevated U concentrations (>300 ppm) made them amenable to in situ laser microprobe techniques. Zircons were mounted in Teflon, with the *c* axis parallel to the mount surface, ground to approximately half-grain thickness, and polished. All zircons were then imaged using optical microscopy (reflected and transmitted light) and CL to detect inclusions and other defects in the crystal lattice and to characterize the distribution of parent nuclides and other elements (*22*, *37*). Structurally complex crystals with various degrees of radiation damage (visible on CL images) were further analyzed by confocal Raman microscopy (WITec alpha300 SAR system with a 2ω-Nd:YAG laser) to quantify the degree of structural disorder (*60*).

He abundance mapping was achieved by repeatedly conducting in situ analysis across the exposed face of the crystal using the protocols described by Evans *et al.* (*17*). An excimer laser (RESOlution M-50A-LR system with a COMPex 102 model) was deployed using square laser spots (13 μm × 13 μm or 9 μm × 9 μm, depending on the intensity of the ^{4}He signal) in a regular grid pattern (fig. S2). Ablations of 8 s at 5 Hz and a fluence of ~1 J cm^{-2} created relatively shallow pits (~1.8 μm deep) with a tetragonal frustum shape. Atomic force microscopy (AFM) was used to determine ablation volumes, which averaged 190 ± 2% (1 SD) μm^3 for the larger spot size (13 μm × 13 μm) and 65 ± 2% (1 SD) μm^3 for the smaller spot size (9 μm × 9 μm). AFM measurement uncertainties were calculated from pit volume data measured on 40 randomly selected pits measured on each crystal. Gas from the ablated material was purified using hot and cold Ti-Zr getters and analyzed for ^{4}He by isotope dilution using a quadrupole mass spectrometer (Pfeiffer PrismaPlus). ^{4}He content was corrected for blank and H interferences. Typical blank values are 0.0025 ncc (at standard temperature and pressure), which allows us to measure the ^{4}He signal at the 0.001 ncc level with a precision of <6% (1 σ). This uncertainty on individual ^{4}He measurements (typically 3 to 6%) was calculated as the square root of the sum of the squares of the precision of the ^{4}He gas standard, the precision of the ^{4}He/^{3}He after blank subtraction, and the precision of the gas standard volume calibration.

After He measurement, zircon crystals were repolished to remove the ~2-μm layer of ablated material, loaded into a flow-through cell, and ablated a second time to measure the concentration of U, Th, and Pb isotopes and a range of other trace elements by LA-ICPMS (Agilent 7700s). The zircons were ablated for 30 s at 5 Hz and at a fluence of 1.5 J cm^{-2} using 15-μm circular spots, arranged in a regular grid (15 μm × 15 μm). NIST 610 and 612 glass standards were used to calculate elemental concentrations (using ^{29}Si as the internal standard element) and to correct for instrument drift. For U-Pb age determination, the primary age standard was 91500 (*61*), with GJ-1 run as an unknown to verify the procedure (*62*). Trace element and U-Pb laser data were processed using Iolite (*63*) and in-house MS Excel macros. Results of all laser ablation spot analyses were transformed into maps using a kriging algorithm in Golden Software Surfer version 8. After the LA-ICPMS spot analyses, the remaining parts of the crystals were removed from the Teflon mount and analyzed by conventional (U-Th)/He methods, following the protocols described by Danišík *et al.* (*64*).

SUPPLEMENTARY MATERIALS

Supplementary material for this article is available at http://advances.sciencemag.org/cgi/content/full/3/2/e1601121/DC1

fig. S1. U-Pb Concordia diagrams.

fig. S2. Ablation pits.

table S1. He and eU data used for maps.

table S2. U-Pb analytical data.

REFERENCES AND NOTES

1. J. M. Rahl, P. W. Reiners, I. H. Campbell, S. Nicolescu, C.M. Allen, Combined single-grain (U-Th)/He and U/Pb dating of detrital zircons from the Navajo Sandstone, Utah. *Geology* **31**, 761–764 (2003).
2. K. Min, P. W. Reiners, S. Nicolescu, J. P. Greenwood, Age and temperature of shock metamorphism of Martian meteorite Los Angeles from (U-Th)/He thermochronometry. *Geology* **32**, 677–680 (2004).

3. B. I. A. McInnes, N. J. Evans, F. Q. Fu, S. Garwin, Application of thermochronology to hydrothermal ore deposits, *Rev. Mineral. Geochem.* **58**, 467–498 (2005).
4. P. W. Reiners, M. T. Brandon, Using thermochronology to understand orogenic erosion. *Annu. Rev. Earth Planet. Sci.* **34**, 419–466 (2006).
5. P. W. Reiners, Thermochronologic approaches to paleotopography. *Rev. Mineral. Geochem.* **66**, 243–267 (2007).
6. A. K. Schmitt, M. Danišík, N. J. Evans, W. Siebel, E. Kiemele, F. Aydin, J. C. Harvey, Acigöl rhyolite field, Central Anatolia (part 1): High-resolution dating of pre-eruptive zircon residence and rhyolite eruption episodes. *Contrib. Mineral. Petrol.* **162**, 1215–1231 (2011).
7. M. C. van Soest, K. V. Hodges, J. A. Wartho, M. B. Biren, B. D. Monteleone, J. Ramezani, J. G. Spray, L. M. Thompson, (U-Th)/He dating of terrestrial impact structures: The Manicouagan example. *Geochem. Geophys. Geosyst.* **12**, Q0AA16 (2011).
8. N. J. Evans, B. I. A. McInnes, B. J. McDonald, M. Danišík, F. Jourdan, C. Mayers, E. Thern, D. Corbett, Emplacement age and thermal footprint of the diamondiferous Ellendale E9 lamproite pipe, Western Australia. *Miner. Depos.* **48**, 413–421 (2013).
9. P. W. Reiners, T. L. Spell, S. Nicolescu, K. A. Zanetti, Zircon (U–Th)/He thermochronometry: He diffusion and comparisons with $^{40}Ar/^{39}Ar$ dating. *Geochim. Cosmochim. Acta* **68**, 1857–1887 (2004).
10. W. R. Guenthner, P. W. Reiners, R. A. Ketcham, L. Nasdala, G. Giester, Helium diffusion in natural zircon: Radiation damage, anisotropy, and the interpretation of zircon (U–Th)/He thermochronology. *Am. J. Sci.* **313**, 145–198 (2013).
11. K. A. Farley, (U–Th)/He dating: Techniques, calibrations, and applications. *Rev. Mineral. Geochem.* **47**, 819–844 (2002).
12. P. W. Reiners, K. A. Farley, H. Hickes, He diffusion and (U-Th)/He thermochronometry of zircon: Initial results from Fish Canyon Tuff and Gold Butte. *Tectonophysics* **349**, 297–308 (2002).
13. P. W. Reiners, Zircon (U–Th)/He thermochronometry. *Rev. Mineral. Geochem.* **58**, 151–179 (2005).
14. J. W. Boyce, K. V. Hodges, W. J. Olszewski, M. J. Jercinovic, B. D. Carpenter, P. W. Reiners, Laser microprobe (U–Th)/He geochronology. *Geochim. Cosmochim. Acta* **70**, 3031–3039 (2006).
15. P. Vermeesch, S. C. Sherlock, N. M. W. Roberts, A. Carter, A simple method for in situ U-Th-He dating. *Geochim. Cosmochim. Acta* **79**, 140–147 (2012).
16. A. Tripathy-Lang, K. V. Hodges, B. Monteleone, M. van Soest, Laser (U-Th)/He thermochronology of detrital zircons as a tool for studying surface processes in modern catchments. *J. Geophys. Res.* **118**, 1333–1341 (2013).
17. N. J. Evans, B. I. A. McInnes, B. McDonald, M. Danišík, T. Becker, P. Vermeesch, M. Shelley, E. Marillo-Sialer, D. B. Patterson, An in situ technique for (U–Th–Sm)/He and U-Pb double dating. *J. Anal. At. Spectrom* **30**, 1636–1645 (2015).
18. A. M. Horne, M. C. van Soest, K. V. Hodges, A. Tripathy-Lang, J. K. Hourigan, Integrated single crystal laser ablation U/Pb and (U-Th)/He dating of detrital accessory minerals—Proof-of-concept studies of titanites and zircons from the Fish Canyon Tuff. *Geochim. Cosmochim. Acta* **178**, 106–123 (2016).
19. D. L. Shuster, K. A. Farley, $^{4}He/^{3}He$ Thermochronometry. *Earth Planet. Sci. Lett.* **217**, 1–17 (2004).
20. D. L. Shuster, K. A. Farley, J. M. Sisterson, D. S. Burnett, Quantifying the diffusion kinetics and spatial distributions of radiogenic ^{4}He in minerals containing proton-induced ^{3}He. *Earth Planet. Sci. Lett.* **217**, 19–32 (2004).
21. A. Tripathy-Lang, M. Fox, D. L. Shuster, Zircon $^{4}He/^{3}He$ thermochronometry. *Geochim. Cosmochim. Acta* **166**, 1–14 (2015).
22. K. H. Dobson, F. M. Stuart, T. J. Dempster; EIMF, U and Th zonation in Fish Canyon Tuff zircons: Implications for a zircon (U–Th)/He standard. *Geochim. Cosmochim. Acta* **72**, 4545–4755 (2008).
23. P. W. Reiners, I. H. Campbell, S. Nicolescu, C. M. Allen, J. K. Hourigan, J. I. Garver, J. M. Mattinson, D. S. Cowan, (U-Th)/(He-Pb) double dating of detrital zircons. *AJS Online* **305**, 259–311 (2005).
24. V. Hurai, M. Danišík, M. Huraiová, J.-L. Paquette, A. Ádám, Combined U/Pb and (U-Th)/He geochronometry of basalt maars in Western Carpathians: Implications for age of intraplate volcanism and origin of zircon metasomatism. *Contrib. Mineral. Petrol.* **166**, 1235–1251 (2013).
25. A. Weisheit, P. Bons, M. Danišík, M. Elburg, Crustal-scale folding: Palaeozoic deformation of the Mt. Painter Inlier, South Australia. *Geol. Soc. Spec. Publ.* **394**, 53–77 (2013).
26. A. Sobczyk, M. Danišík, P. Aleksandrowski, A. Anczkiewicz, Post-Variscan cooling history of the central Western Sudetes (NE Bohemian Massif, Poland) constrained by apatite fission-track and zircon (U-Th)/He thermochronology. *Tectonophysics* **649**, 47–57 (2015).
27. C. W. Magee Jr., M. Danišík, T. Mernagh, Extreme isotopologue disequilibrium in molecular SIMS species during SHRIMP geochronology. *Geosci. Instrum. Method. Data Syst.* **2016**, 1–29 (2016).
28. K. A. Farley, Helium diffusion from apatite: General behavior as illustrated by Durango fluorapatite. *J. Geophys. Res.* **105**, 2903–2914 (2000).
29. K. A. Farley, R. A. Wolf, L. T. Silver, The effects of long alpha-stopping distances on (U–Th)/He ages. *Geochim. Cosmochim. Acta* **60**, 4223–4229 (1996).
30. J. K. Hourigan, P. W. Reiners, M. T. Brandon, U-Th zonation-dependent alpha-ejection in (U–Th)/He chronometry. *Geochim. Cosmochim. Acta* **69**, 3349–3365 (2005).
31. C. Gautheron, L. Tassan-Got, R.-A. Ketcham, K. J. Dobson, Accounting for long alpha-particle stopping distances in (U–Th–Sm)/He geochronology: 3D modeling of diffusion, zoning, implantation, and abrasion. *Geochim. Cosmochim. Acta* **96**, 44–56 (2012).
32. R. W. Brown, R. Beucher, S. Roper, C. Persano, F. Stuart, P. Fitzgerald, Natural age dispersion arising from the analysis of broken crystals. Part I: Theoretical basis and implications for the apatite (U–Th)/He thermochronometer. *Geochim. Cosmochim. Acta* **122**, 478–497 (2013).
33. D. A. Orme, P. W. Reiners, J. K. Hourigan, B. Carrapa, Effects of inherited cores and magmatic overgrowths on zircon (U-Th)/He ages and age-eU trends from Greater Himalayan sequence rocks, Mount Everest region, Tibet. *Geochem. Geophys. Geosyst.* **16**, 2499–2507 (2015).
34. P. M. Hurley, Alpha ionization damage as a cause of low He ratios. *Eos. Trans. AGU* **33**, 174–183 (1952).
35. H. J. Lippolt, M. Leitz, R. S. Wernicke, B. Hagedorn, (Uranium + thorium)/helium dating of apatite: Experience with samples from different geochemical environments. *Chem. Geol.* **112**, 179–191 (1994).
36. D. F. Stockli, K. A. Farley, T. Dumitru, Calibration of the (U-Th)/He thermochronometer on an exhumed fault block, White Mountains, California. *Geology* **28**, 983–986 (2000).
37. M. Jolivet, T. Dempster, R. Cox, Distribution of U and Th in apatites: Implications for U–Th/He thermochronology. *C. R. Geosci.* **335**, 899–906 (2003).
38. F. Stuart, G. Turner, R. Taylor, He–Ar isotope systematics of fluid inclusions: Resolving mantle and crustal contributions to hydrothermal fluids, in *Noble Gas Geochemistry and Cosmochemistry* (Terra Scientific Publishing Company, 1994), pp. 261–277.
39. D. M. Djimbi, C. Gautheron, J. Roques, L. Tassan-Got, C. Gerin, E. Simoni, Impact of apatite chemical composition on (U-Th)/He thermochronometry: An atomistic point of view. *Geochim. Cosmochim. Acta* **167**, 162–176 (2015).
40. D. L. Shuster, R. M. Flowers, K. A. Farley, The influence of natural radiation damage on helium diffusion kinetics in apatite. *Earth Planet. Sci. Lett.* **249**, 148–161 (2006).
41. T. A. Ehlers, K. A. Farley, Apatite (U–Th)/He thermochronometry: Methods and applications to problems in tectonic and surface processes. *Earth Planet. Sci. Lett.* **206**, 1–14 (2003).
42. E. B. Watson, D. J. Cherniak, Lattice diffusion of Ar in quartz, with constraints on Ar solubility and evidence of nanopores. *Geochim. Cosmochim. Acta* **67**, 2043–2062 (2003).
43. A. G. C. A. Meesters, T. J. Dunai, Solving the production–diffusion equation for finite diffusion domains of the various shapes: Part 1. Implications for low temperature (U–Th)/He thermochronology. *Chem. Geol.* **186**, 333–344 (2002).
44. A. G. C. A. Meesters, T. J. Dunai, Solving the production–diffusion equation for finite diffusion domains of various shapes: Part 2. Application to cases with α ejection and non-homogeneous distribution of the source. *Chem. Geol.* **186**, 345–363 (2002).
45. E. A. Bargnesi, D. F. Stockli, J. K. Hourigan, C. Hager, Improved accuracy of zircon (U–Th)/He ages by rectifying parent nuclide zonation with practical methods. *Chem. Geol.* **426**, 158–169 (2016).
46. K. A. Farley, D. L. Shuster, R. A. Ketcham, U and Th zonation in apatite observed by laser ablation ICPMS, and implications for the (U–Th)/He system. *Geochim. Cosmochim. Acta* **75**, 4515–4530 (2011).
47. M. Danišík, P. Shane, A. K. Schmitt, A. Hogg, G. M. Santos, S. Storm, N. J. Evans, L. K. Fifield, J. M. Lindsay, Re-anchoring the late Pleistocene tephrochronology of New Zealand based on concordant radiocarbon ages and combined $^{238}U/^{230}Th$ disequilibrium and (U–Th)/He zircon ages. *Earth Planet. Sci. Lett.* **349–350**, 240–250 (2012).
48. M. Danišík, A. K. Schmitt, D. F. Stockli, O. M. Lovera, I. Dunkl, N. J. Evans, Application of combined U-Th-disequilibrium/U-Pb and (U-Th)/He zircon dating to tephrochronology. *Quat. Geochronol.* 10.1016/j.quageo.2016.07.005 (2016).
49. R. M. Flowers, R. A. Ketcham, D. L. Shuster, K. A. Farley, Apatite (U–Th)/He thermochronometry using a radiation damage accumulation and annealing model. *Geochim. Cosmochim. Acta* **73**, 2347–2365 (2009).
50. P. Rossi, A. Cocherie, Genesis of a Variscan batholith: Field, petrological and mineralogical evidence from the Corsica-Sardinia batholith. *Tectonophysics* **195**, 319–346 (1991).
51. C. Clark, M. Santosh, R. Taylor, I. Fitzsimons, V. Nandakumar, E. Shaji, *Granulites and Granulites 2013—Field Guide to the Charnockites, Khondalites and Leptynotes of the Kerala Khondalite Belt, Southern Granulite Terrane, India, 21–26 January 2013* (Curtin University, 2013).

52. R. Kryza, C. Pin, T. Oberc-Dziedzic, Q. G. Crowley, A. Larionov, Deciphering the geochronology of a large granitoid pluton (Karkonosze Granite, SW Poland): An assessment of U–Pb zircon SIMS and Rb–Sr whole rock dates relative to U–Pb zircon CA-ID-TIMS. *Int. Geol. Rev.* **56**, 756–782 (2014).
53. F. Albarède, The recovery of spatial isotope distributions from step-wise degassing data. *Earth Planet. Sci. Lett.* **39**, 387–397 (1978).
54. D. J. Cherniak, E. B. Watson, J. B. Thomas, Diffusion of helium in zircon and apatite. *Chem. Geol.* **268**, 155–166 (2009).
55. E. B. Watson, K. H. Wanser, K. A. Farley, Anisotropic diffusion in a finite cylinder, with geochemical applications. *Geochim. Cosmochim. Acta* **74**, 614–633 (2010).
56. M. G. Malusà, M. Danišík, J. Kuhlemann, Tracking the Adriatic-slab travel beneath the Tethyan margin of Corsica–Sardinia by low-temperature thermochronometry. *Gondw. Res.* **31**, 135–149 (2015).
57. G. Wagner, P. Van den haute, *Fission-Track Dating* (Springer Science and Business Media, 1992).
58. R. A. Wolf, K. A. Farley, D. M. Kass, Modeling of the temperature sensitivity of the apatite (U–Th)/He thermochronometer. *Chem. Geol.* **148**, 105–114 (1998).
59. R. A. Ketcham, Forward and inverse modeling of low-temperature thermochronometry data low-temperature thermochronology: Techniques, interpretations, and applications. *Rev. Mineral. Geochem.* **58**, 275–314 (2005).
60. L. Nasdala, G. Irmer, D. Wolf, The degree of metamictization in zircon: A Raman spectroscopic study. *Eur. J. Mineral.* **7**, 471–478 (1995).
61. M. Wiedenbeck, J. M. Hanchar, W. H. Peck, P. Sylvester, J. Valley, M. Whitehouse, A. Kronz, Y. Morishita, L. Nasdala, J. Fiebig, I. Franchi, J.-P. Girard, R. C. Greenwood, R. Hinton, N. Kita, P. R. D. Mason, M. Norman, M. Ogasawara, P. M. Piccoli, D. Rhede, H. Satoh, B. Schulz-Dobrick, O. Skår, M. J. Spicuzza, K. Terada, A. Tindle, S. Togashi, T. Vennemann, Q. Xie, Y.-F. Zheng, Further characterisation of the 91500 zircon crystal. *Geostand. Geoanal. Res.* **28**, 9–39 (2004).
62. S. E. Jackson, N. J. Pearson, W. L. Griffin, E. A. Belousova, The application of laser ablation-inductively coupled plasma-mass spectrometry to in situ U–Pb zircon geochronology. *Chem. Geol.* **211**, 47–69 (2004).
63. C. Paton, J. D. Woodhead, J. C. Hellstrom, J. M. Hergt, A. Greig, R. Maas, Improved laser ablation U-Pb zircon geochronology through robust downhole fractionation correction. *Geochem. Geophys. Geosyst.* **11**, Q0AA06 (2010).
64. M. Danišík, P. Štěpančíková, N. J. Evans, Constraining long-term denudation and faulting history in intraplate regions by multisystem thermochronology: An example of the Sudetic Marginal Fault (Bohemian Massif, central Europe). *Tectonics* **31**, TC2003 (2012).

Acknowledgments: We acknowledge the help of K. Merigot and A. Halfpenny (Microscopy and Microanalysis Facility, John de Laeter Centre, Curtin University) with polishing and scanning electron microscopy imaging; the advice of M. Shelley and B. Godfrey; the provision of zircon by R. Taylor; and constructive comments by K. Hodges, P. Reiners, and four anonymous reviewers. **Funding:** GeoHistory Facility instruments were funded via an Australian Geophysical Observing System grant provided to AuScope Pty Ltd. by the Australian Education Investment Fund (Round 3) program. M.D. was funded by the AuScope NCRIS2 program, Australian Scientific Instruments Pty Ltd., and Australian Research Council (ARC) Discovery funding scheme (DP160102427). N.J.E. was supported by a Curtin Senior Research Fellowship ARC Discovery funding scheme (DP160102427). The Microscopy and Microanalysis Facility is partially funded by the university, state, and commonwealth governments. **Author contributions:** B.I.A.M. conceived the research idea. M.D., B.J.M., and C.L.K. designed the experiments. M.D., B.J.M., and T.B. performed the experiments. M.D., C.L.K., N.J.E., and T.B. analyzed the data. M.D., N.J.E., B.J.M., and T.B. contributed reagents/materials/analysis tools. M.D., N.J.E., C.L.K., and B.I.A.M. wrote the paper. **Competing interests:** The authors declare that they have no competing interests. **Data and materials availability:** All data will be stored and freely available at the Curtin University library. All data needed to evaluate the conclusions in the paper are present in the paper and/or the Supplementary Materials. Additional data related to this paper may be requested from the authors.

Submitted 18 May 2016
Accepted 10 January 2017
Published 10 February 2017
10.1126/sciadv.1601121

Citation: M. Danišík, B. I. A. McInnes, C. L. Kirkland, B. J. McDonald, N. J. Evans, T. Becker, Seeing is believing: Visualization of He distribution in zircon and implications for thermal history reconstruction on single crystals. *Sci. Adv.* **3**, e1601121 (2017).

Seeing is believing: Visualization of He distribution in zircon and implications for thermal history reconstruction on single crystals

Martin Danisík, Brent I. A. McInnes, Christopher L. Kirkland, Brad J. McDonald, Noreen J. Evans and Thomas Becker

Sci Adv **3** (2), e1601121.
DOI: 10.1126/sciadv.1601121